

Solar image restoration by use of multi-frame blind deconvolution with multiple objects and phase diversity

Michiel van Noort (noort@astro.uio.no)

Luc Rouppe van der Voort (rouppe@astro.uio.no)

Institute of Theoretical Astrophysics, University of Oslo

P.O. Box 1029 Blindern, N-0315 Oslo, Norway

Center of Mathematics for Applications, University of Oslo

P.O. Box 1053 Blindern, N-0316 Oslo, Norway

Mats G. Löfdahl (mats@astro.su.se)

Institute for Solar Physics of the Royal Swedish Academy of Sciences

AlbaNova University Center, SE-106 91 Stockholm, Sweden

March 21, 2005 – (*Version 1.66, momfpd: 2005/03/21, 20:29:41 UT*)

Abstract. An extension on Joint Phase Diverse Speckle image restoration is presented. Multiple realizations of multiple objects having known wavefront relations with each other can now be restored jointly. As the alignment of the imaging setup does not change, near-perfect alignment can be achieved between different objects, thus greatly reducing false signals in the determination of derived quantities, such as magnetograms, Dopplergrams, etc.

The method was implemented in C++ as an image restoration server, to which worker clients can connect and disconnect randomly, so that a large number of CPUs can be used to speed up the restorations.

We present a number of examples of applications of the restoration method to observations obtained with the Swedish 1-m Solar Telescope on La Palma.

Keywords: methods:numerical—image restoration—wavefront sensing

1. Introduction

Seeing is the primary obstacle to obtaining high resolution solar observations from the ground. Turbulence in the atmosphere along the line of sight randomly distorts the wavefronts. The result is blurring and geometrical distortions in the collected images. Solar adaptive optics (AO; Rimmele, 2000; Scharmer et al. 2000) facilitates solar imaging with significantly reduced low-order aberrations. However, due to the time scale of seeing evolution, AO only manages limited high-order corrections. The single wavefront sensor of current AO systems also limits their optimal correction to the isoplanatic patch surrounding the field of view of the wavefront sensor.

Post-facto image restoration techniques can correct higher order aberrations because they do not suffer from the time constraints involved in the AO control system. Anisoplanatic aberrations, whether



© 2005 Kluwer Academic Publishers. Printed in the Netherlands.

partly corrected by AO or not, are easily handled by separate processing of subfields smaller than the isoplanatic patch and mosaicking of the restored subimages. The two most commonly used methods for solar image restoration are Speckle interferometry (de Boer et al., 1992; von der Lühe, 1993) and Phase Diversity (PD) methods (Gonsalves, 1982; Paxman et al., 1992a; Löfdahl and Scharmer, 1994). Both methods have their limitations but have been used to good effect for studying small scale solar structure, see e.g. the work by Keller (1992) and von der Lühe (1994) or, more recently, Sütterlin et al. (2004), Al et al. (2004), and Janßen et al. (2003) for Speckle and by Berger et al. (1998a, 1998b), Tritschler and Schmidt (2002b), Scharmer et al. (2002), and Rouppe van der Voort et al. (2004) for PD.

Speckle interferometry relies on known statistics of the atmospheric turbulence and the assumption that telescopic aberrations are small in comparison. Because of the statistical approach, many frames (~ 100) are needed, necessitating large disk storage or real-time processing (Denker et al., 2001). For large current and future apertures, great demands are also put on camera read-out speed as the solar evolution time decreases with increasing angular resolution. AO correction is crucial for larger telescopes, which presents a challenge for Speckle methods. While Denker et al. (2004) recently demonstrated that Speckle can well estimate the Fourier phase (encoding the morphology) of AO corrected solar images, they also show that the restored power spectrum is not correctly estimated because of the way AO correction modifies the statistics of the atmospheric turbulence. This is hopefully a passing problem, since e.g. Sailer et al. (2004) are working on including AO correction in the calculations of the Speckle transfer function.

Phase Diversity (PD) methods (Gonsalves, 1982; Paxman et al., 1992a; Löfdahl and Scharmer, 1994), phase diverse speckle (PDS) methods (Paxman et al., 1992b; Paxman et al., 1996), and some approaches to Multi-Frame Blind Deconvolution (MFBD; Schulz, 1993; Van Kampen and Paxman, 1998) jointly estimate the un-aberrated object as well as the pupil phase aberrations responsible for the blurring in a Maximum Likelihood sense. We will collectively refer to all these methods as MFBD methods. A small number ($\lesssim 10$) of realizations of the random atmospheric turbulence is usually sufficient for good restorations. (In fact, speckle interferometry would not be very useful with the short collection intervals ($\lesssim 10$ s, the solar evolution time, assuming a sound speed on the Sun of ~ 7 km/s and a telescope resolution of $0''.1$) and slow cameras ($\lesssim 4$ frames/s) we use in this paper.) The reason is that MFBD does not rely on statistics at all. Instead, a simple model of the optics, including its unknown pupil phase, and the detectors is used. Such models are fairly robust for telescopes with a clear, circular aperture.

However, for telescopes with a partly obscured and/or variable pupil, a model can be more difficult to make, with unknown consequences for the accuracy of the restorations. The information needed for separating the object and the aberrations comes from diversity that encodes the information about the object and the instantaneous wavefronts at the times of exposure in linearly independent ways. By diversity we here refer to the known diversity used by PD methods, usually realized by defocusing a camera, as well as the unknown, randomly variable diversity created by the seeing. MFBD methods do not make any distinction between seeing and telescopic aberrations, and therefore they have no problem with partial and space-variant AO-correction. However, with or without AO corrected data, the power spectra of images restored with MFBD methods suffer from the finite expansion of the pupil phases, causing a systematic underestimation of the wings of the PSFs (Roupe van der Voort et al., 2004).

MFBD methods work best when the contrast is high, the noise is low and the exposure time is short. However, these are properties that are difficult to achieve simultaneously for narrow-band solar filtergrams. Keller and von der Lühe (1992) collected wideband data simultaneously with very noisy narrow band data, using the PSFs from speckle processing of the former to restore the latter. For more recent results with similar processing, see e.g. Al et al. (2004), Rutten et al. (2004), and Janßen et al. (2003). Löfdahl et al. (1998) used PD-estimated wavefronts from the G-band for deconvolution of simultaneous wideband images, taking fixed aberration differences between the two channels into account. Tritschler and Schmidt (2002a) deconvolved images from several wavelengths with wavefronts estimated from PD data in one wavelength, recognizing that fixed telescopic aberrations and atmospheric aberrations scale differently with wavelength. Evidently, this approach works both for PD and speckle but is suboptimal in the sense that not all available data are used for the estimation of the aberrations.

PD and PDS are generalizations of MFBD. Löfdahl (2002) recognized that further generalizations are possible. The method we present in this paper is such a generalization, that allows joint processing of multiple MFBD data sets with different objects, while benefiting from PD. We use the term “different objects” in an image processing sense, referring to the same location of the solar surface, but viewed through different filters or polarizers. In addition to providing better wavefront sensing than with separate processing of the MFBD data sets, the joint processing also makes possible a novel approach for achieving virtually perfect registration of the different imaging channels. This helps considerably with further processing involving differences of image channels, such as making magnetograms and Dopplergrams.

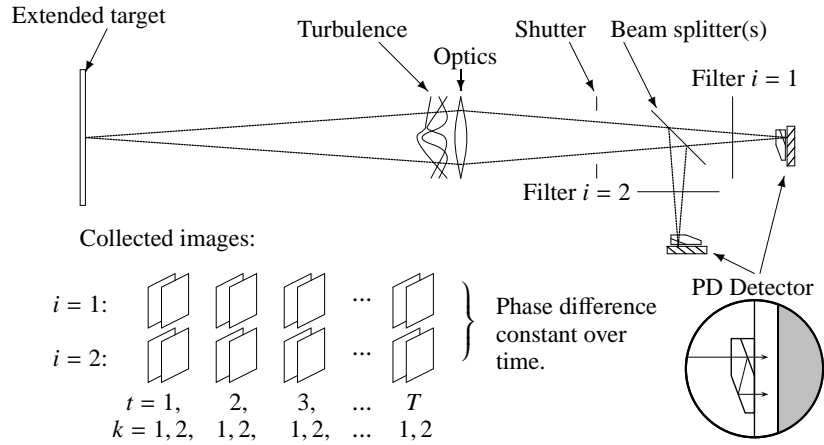


Figure 1. Data collection model. All images collected at a particular time, t , share the same realization of the random seeing phase aberrations. The “filters” can be interference filters or polarizers, depending on the observational needs. Although looking at the same patch on the Sun, they give rise to different objects, i . A “PD detector” is either a set of cameras and beamsplitters that collect images at different focus positions (as in Section 4.1 below) or a device that lets us collect such images on a single camera (see circular inset). The diversity channels are labeled with different k .

Earlier work in the area of combining multi-spectral data for wavefront sensing and image restoration include the wavelength diversity simulation experiments by Thelen et al. (1995) and Dionne and Gonçalves (2004), who assume a common object (up to a scale factor) in the wavefront sensing step. For well separated wavelengths, it has the attractive property of providing phase diversity (by wavelength change instead of focus shift). It is not useful for solar observations, because the assumption of a common object involves a model mismatch that should give suboptimal fitting for targets like the Sun, where the whole point of multi-wavelength observations is that the Sun looks different. Furthermore, the assumption of a common wavefront deformation breaks down for atmospheric turbulence when the wavelengths are too much separated. Ingleby and McGaughey (2005) use a multiple object approach more similar to our processing of solar data, although it is not clear from the published data whether their performance is actually better than single-object MFB.

2. Algorithm

2.1. DATA COLLECTION MODEL

Figure 1 shows an idealized optical setup, illustrating the data collection model used in this paper. An extended target, like a part of the solar surface, is observed through atmospheric turbulence and an aberrated optical system, including the intentional aberrations introduced by an AO system, designed to partly compensate for the atmospheric aberrations.

There are several detectors, synchronized with an external shutter. For images collected at the same instant, $t \in \mathcal{T}_i$, they all sample the same realization of the random atmospheric turbulence and they all see the same aberrations in the optics up to the beamsplitter. The filters (the term is used collectively for interference filters and polarizers) change the object but not the aberrations before the beamsplitter (as long as the wavelength difference is not too large). The multiple objects are denoted by f_i , where $i \in \{1, \dots, I \geq 1\}$. Each object is simultaneously imaged in a number of focus diversity channels, indicated with an index $k \in \mathcal{K}_i$. For the example setup in the figure, $I = 2$, $\mathcal{K}_i = \{1, 2\}$, and $\mathcal{T}_i = \{1, \dots, T\}$.

For notational ease, we will begin with a shorthand where the two indices t and k are collapsed into a single index $j \in \mathcal{J}_i = \mathcal{T}_i \times \mathcal{K}_i$.

We use a space invariant image formation model with Gaussian white noise. A data frame d_{ij} can then be expressed as the convolution of an object, f_i , and a point spread function (PSF), s_{ij} , plus a noise frame with Gaussian statistics, n_{ij} . In the Fourier domain we get

$$D_{ij}(u) = F_i(u) \cdot S_{ij}(u) + N_{ij}(u), \quad (1)$$

where the uppercase symbols are the Fourier transforms of their lower case counterparts and u is the 2-D spatial frequency coordinate. For brevity, we will drop this coordinate for the remainder of the paper. The space invariance is violated by anisoplanatism, so for a large field of view, the model is restricted to separate processing of subfields that are smaller than or on the order of the isoplanatic angle.

The optical transfer function (OTF) can be written as

$$S_{ij} = \mathfrak{F}\{|\mathfrak{F}^{-1}\{P_{ij}\}|^2\}, \quad (2)$$

where \mathfrak{F} is the Fourier transform operator. P_{ij} is the generalized pupil function that characterizes the optical system,

$$P_{ij} = A_{ij} \exp\{i\phi_{ij}\}, \quad (3)$$

where ϕ_{ij} is the pupil phase, A_{ij} is a usually binary function that specifies the pupil transmission (and thereby its geometrical extent), and $i = \sqrt{-1}$.

We parameterize the unknown phases,

$$\phi_{ij} = \theta_{ij} + \sum_{m \in \mathcal{M}} \alpha_{ijm} \psi_{im}, \quad (4)$$

where θ_{ij} is used for known phase differences, such as focus diversities, subpixel registration, and fixed aberration differences, see below. \mathcal{M} is the set of mode indices. The set of basis functions, $\{\psi_{im}\}$, can be chosen depending on the problem to be solved.

For optical elements, Zernike polynomials (Noll, 1976) are ideal but for atmospheric turbulence, we use a combination of Zernike (Z) polynomials for registration and atmospheric Karhunen–Loève (KL) modes (Roddier, 1990) for the blurring effects,

$$\psi_{im} = \begin{cases} Z_m/\lambda_i; & m \in \mathcal{M}_{\text{tilts}}, \\ \text{KL}_m/\lambda_i; & m \in \mathcal{M}_{\text{blur}}. \end{cases} \quad (5)$$

With the numbering scheme of Noll (1976), we have $\mathcal{M} = \mathcal{M}_{\text{tilts}} \cup \mathcal{M}_{\text{blur}}$, where $\mathcal{M}_{\text{tilts}} = \{2, 3\}$ and $\mathcal{M}_{\text{blur}} = \{4, \dots, M\}$. The modes are normalized with respect to the wavelength used for f_i so identical α_{ijm} coefficients at different wavelengths correspond to the same wavefront or translation.

We lexicographically arrange all the α_{ijm} in a single column vector,

$$\boldsymbol{\alpha} = [\boldsymbol{\alpha}_1 \ \boldsymbol{\alpha}_2 \ \dots \ \boldsymbol{\alpha}_I]^\text{T}, \quad (6)$$

where T used as a superscript denotes matrix transpose and

$$\boldsymbol{\alpha}_i = [\dots \ \alpha_{ijm} \ \dots]_{j,m \in \mathcal{J}_i \times \mathcal{M}}^\text{T}. \quad (7)$$

2.2. CONSTRAINED MFBD

For each object i , the data collection model describes a data set that can be processed with MFBD. There are different approaches to doing this. We use the one by Schulz (1993), where we jointly estimate the object and the aberrations that minimize a Maximum Likelihood error metric that measures the difference between the data frames and model data frames based on the estimated quantities. The mathematical form of the metric depends on the noise statistics. The simplest metric and the fastest code is obtained for additive Gaussian noise statistics, which happens to be a good approximation for low-contrast objects like the

solar photosphere. It is not as good for high-contrast wavelengths, particularly when we are photon starved (see Section 4.4 below). The Gaussian metric is a least squares difference between a data frame D_{ij} and the corresponding estimated quantity, $\hat{F}_i \hat{S}_{ij}$, where the caret denotes an estimated quantity. This can be simplified to a metric that does not explicitly involve the object (Paxman et al., 1996),

$$L_i(\boldsymbol{\alpha}_i) = \sum_u \left[\sum_j^J |D_{ij}|^2 - \frac{|\sum_j^J D_{ij}^* \hat{S}_{ij}|^2}{\sum_j^J |\hat{S}_{ij}|^2 + \gamma_i} \right]. \quad (8)$$

The γ_i term is proportional to the noise power and corresponds to a simple Wiener filter. In practice, we have been using Scharmer's optimum low pass filter for this step (Löfdahl et al., 1998).

The solution to the MFBD problem is to find the $\boldsymbol{\alpha}$ that minimizes L and thereby also the MFBD estimate of the object. Standard optimization algorithms can be used. This involves iterative methods and usually calculation of gradients with respect to the metric. These and other details are described by Löfdahl (2002).

If nothing else is known, the pupil phases are independent. However, we can refine the mathematical description of the data collection model by specifying linear equality constraints (LECs) on the pupil phase coefficients and thereby reducing the number of effectively unknown parameters. The constraints are given as a set of linear equations that have to be satisfied exactly while L is minimized.

One example is PDS. By exposing multiple cameras, looking through the same telescope, simultaneously, a set of images can be obtained for which the degradation of the images due to atmospheric distortions is identical. By focusing the cameras differently, we introduce a known phase difference. This can be modeled as a focus (Z_4) contribution to θ_{ij} in Eq. (4). The remainder of the aberrations in PD channels are the same, so we initialize the optimization with $\boldsymbol{\alpha} = \boldsymbol{\alpha}_i \equiv 0$ and constrain the changes in the wavefront coefficients to be identical for all images in the set, i.e. $\forall i$,

$$\alpha_{it1m} - \alpha_{itkm} = 0; \quad k > 1, m \in \mathcal{M}. \quad (9a)$$

The modes $m \in \mathcal{M}_{\text{tilts}}$ need another kind of constraint, because the algorithm is insensitive to a global shift and because the tilt estimation has to deal with other means of registering the subimages. In addition to Eq. (9a), we require the registration parameters for the focus channel to sum to zero,

$$\sum_t \alpha_{itkm} = 0; \quad m \in \mathcal{M}_{\text{tilts}}. \quad (9b)$$

In Section 4 below we say that two (or more) frames are *linked* when we have constrained the relation between the aberration coefficients of the frames.

We write the constraints (Here: Eqs. (9a) and (9b)) in matrix form,

$$\mathbf{C} \cdot \boldsymbol{\alpha} = 0. \quad (10)$$

This equation is under-determined so there is no unique solution. All solutions to Eq. (10) can be written as

$$\boldsymbol{\alpha} = \mathbf{Q}_2 \cdot \boldsymbol{\beta}, \quad (11)$$

where the column vectors of \mathbf{Q}_2 are an orthogonal basis of the null space of \mathbf{C} . This is now the space available for optimization. The constrained minimization problem in $\boldsymbol{\alpha}$ is transformed into an unconstrained minimization problem in a reduced set of variables, $\boldsymbol{\beta}$, that are linear combinations of the original coefficients. Each constraint reduces the number of unknowns by one. This helps by increasing the amount of measured data per estimated quantity, thereby making the problem better determined.

The non-linear minimization problem in the reduced set of parameters can still be treated with standard methods. The theory for solving optimization problems with LECs can be found in some text books on numerical methods, e.g. the one by Kahaner et al. (1989).

2.3. REGISTRATION

In Section 2.1, the only difference between the realizations of a single object is assumed to be in the wavefronts. As the isoplanatic patches are fairly small, special care needs to be taken with the registration of subimages, i.e. with the α_{itkm} coefficients for $m \in \mathcal{M}_{\text{tilts}}$. If these coefficients become large, a significant fraction of the pixels in the corresponding subfield will wrap around to the other side, a direct consequence of the assumption of periodicity in the Fourier transform. The subimage therefore really represents a different object, which can result in incorrect restorations, particularly in areas with large scale intensity gradients (such as sunspots and large pores).

The tilts should therefore be realized as far as possible in terms of a shift in the image coordinates, from where the subimage is read. Cross correlation of degraded solar data can serve as a first approximation, but is not necessarily the correct alignment for the object because the PSF of the observed data may not be symmetric. Registration and the corresponding refinement of the subfield coordinates therefore needs to be part of the wavefront sensing process. This can be readily done by splitting up the iterative minimization process of Section 2.2

in several steps, where the convergence criterion is reduced and the number of fitted modes increased in consecutive iterations until the desired convergence is reached. Between each of these iteration steps, the tilt coefficients are converted to pixel shifts, and a new subimage is cut out from the raw image at the corrected location, rounded to the nearest pixel. The tilt coefficient is then corrected for the shift effectively applied to the patch and taken as the starting value in the next iteration.

Depending on the amount of differential seeing, typically 3–4 such steps are needed to obtain a stack of subimages that are aligned to within one pixel.

2.4. MULTIPLE OBJECTS

When $I > 1$, we have several MFBD data sets corresponding to multiple objects, with or without PD.

The wavefronts are again identical for simultaneous images, except for diversity and possibly known fixed aberration differences. Identical wavefronts does not mean that the PSF of the system of atmosphere and telescope combined is identical, as there may be influences of the difference in the wavelength at which the images are taken, but rather that the wavefront arriving at the telescope is identical for each image in the set.

Clearly, minimizing the individual metrics, L_i , also minimizes the weighted sum of the individual object metrics,

$$L = \sum_i w_i L_i. \quad (12)$$

Except for convergence issues, we could run a single optimization problem minimizing L by varying $\boldsymbol{\alpha}$ and we would get the same results as when minimizing the individual L_i by varying the $\boldsymbol{\alpha}_i$. We can, however, formulate additional constraints, that link the different objects, in the same way that diversity channels are linked to each other. This is the extended formulation of Löfdahl (2002, Sect. 4), that we have implemented and will be using below.

We use the weights $w_i = 1$. It is possible that other weights are better in some cases, experimentation did not show significant improvements for the datasets used in this paper.

3. Implementation

For optimization, we used the BFGS method (Kelley, 1999). Like the more well known conjugate gradients method, it is a quasi-Newton method but more advanced when choosing the next descent direction.

The implementation of the algorithm in section 2.2, coded by Löfdahl (2002) in ANA (Shine et al., 1988), is rather slow. A new implementation was therefore made in C++, which was found to be typically 30 times faster than the original implementation in ANA, while not significantly changing the results.

To the C++ implementation was then added the registration refinements from Section 2.3 and the multiple objects extension from Section 2.4. The code makes use of the open source FFTW library (Frigo and Johnson, 2005) for Fast Fourier transforms.

To keep even very large problems manageable, the code is capable of using a large number of CPUs, connected with a network. CPUs can be added and removed at will and successful operation has thus far been achieved with more than 100 CPUs.

For more information about the code and downloads, see: <http://www.momfbd.org/>

4. Results

In this section, some examples of Multi-Object MFBD (MOMFBD) image restoration applied to real solar data are presented. The observations were obtained with the Swedish 1-m Solar Telescope (SST; Scharmer et al., 2003a) on La Palma. As it is necessary to build a special optical setup to be able to do MOMFBD image restorations, the optical setup is described in some detail below.

4.1. OPTICAL SETUP

The SST re-images the primary focus through a Schupmann system, that removes chromatic aberrations from the 1-m singlet lens. After the Schupmann focus follows a tip-tilt mirror, a deformable bimorph mirror, and a re-imaging lens that adapts the image scale to the cameras used. A dichroic beamsplitter (~ 500 nm) splits the light into a “red” and a “blue” beam. Both beams accommodate scientific cameras and the red beam also has the correlation tracker and a Schack–Hartmann sensor. The tip-tilt mirror, bimorph mirror, correlation tracker and Schack–Hartmann sensors constitute the SST AO system (Scharmer et al., 2003b).

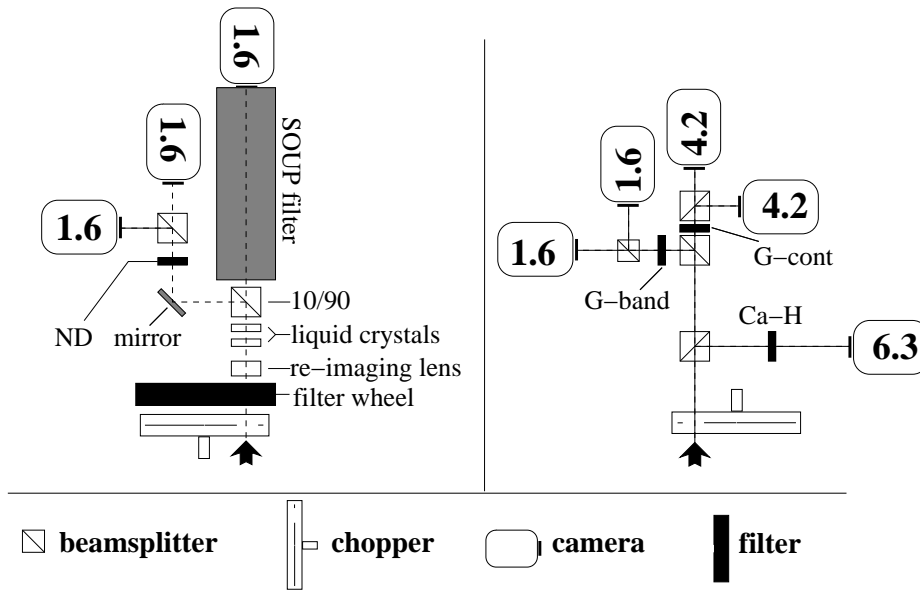


Figure 2. Optical setup for the red (left) and the blue (right) beam. Arrows mark the direction of incoming sun light. Cubic beamsplitters reflect/transmit light according to the ratio 50/50 unless otherwise noted. Cameras are marked 1.6, 4.2, and 6.3 indicating the number of mega-pixels. The beam towards the broad band PD cameras in the red beam has a neutral density (ND) filter to balance the exposure level.

Figure 2 shows the two scientific camera setups, the red setup with the Lockheed Martin Solar Optical Universal Polarimeter (SOUP, Title and Rosenberg, 1981) tunable filter and the blue setup with filters in and around the 430.5 nm G-band, the nearby continuum (“G-cont”) at 436.4 nm and the Ca II H line at 396.9 nm.

All science cameras are from the Kodak/Roper/Redlake Megaplug camera series equipped with KAF-1600, KAF-4200, and KAF-6300 CCD chips. These cameras are full frame CCD cameras with 10-bit readout interface and 10 MHz pixel clock rate.

The key property that makes MOMFBD possible is that a known relation exists between the wavefronts of a set of images. In practice, this is done by exposing cameras simultaneously, so that the recorded images are degraded by the same seeing. Unfortunately, as the cameras are fitted with mechanical shutters with variable characteristics, simultaneous exposure could not be guaranteed by simply synchronizing the exposure trigger signals. Not only do these cameras have a variable response time to an external trigger signal, they also suffer from accel-

eration effects at short exposure times and an unknown/uncontrollable shutter sweep direction, further complicating the data reduction.

To address these problems, the cameras were synchronized by means of an optical chopper. Although a chopper produces a periodic exposure instead of the required single exposure, if the duty cycle of the chopped beam is low enough, it can be used to shorten a longer single exposure if properly synchronized.

In both the red and the blue beam setups (the two setups could not be run synchronized, using a single chopper, as interrupting the main beam interferes with the operation of the AO system), the chopper disc has an open sector with an opening angle of 60° , so the chopped beam has a duty cycle of $\frac{1}{6}$. The exposure window is 35×35 mm at a distance of 52 mm from disc center, corresponding to a rotation angle φ of $\sim 37^\circ$. The camera trigger signals are diverted to a simple logic circuit, designed to hold the trigger signal until all cameras in the setup are triggered, after which a combined trigger signal is generated. This trigger signal is then in turn held, until the chopper signal starts its dark period. This produces a trigger signal that causes all the camera shutters to open, for which they can then use the entire dark period, $1 - \frac{1}{6} - \frac{\varphi}{360}$ of the rotation period, of the chopper. When the chopped beam starts its light period, all cameras are opened and exposed absolutely simultaneously. As the chopper rotates at a constant rate, no acceleration effects are introduced in the signal, resulting in a uniform exposure across the CCD. The start of the next dark period triggers the cameras to close again, for which they again have the entire dark period, as above.

Given a maximum shutter delay of the cameras of 12 ms, the minimum exposure time of this setup is approximately 2 ms.

4.2. CALIBRATION

For good image restoration, sub-pixel alignment of all object cameras is required. Unfortunately, even using the smallest pinholes possible, physically aligning all the cameras could only be achieved to within ~ 0.05 mm, corresponding to approximately 5 pixels on the CCD. As this level of accuracy is not sufficient, the remainder of the misalignment needs to be dealt with numerically.

An accurate estimate of the misalignment of the setup can only be made if all cameras are looking at exactly the same object. Since obviously the Sun looks very different in different wavelength bands, solar images are not suitable for calibration. Removing all filters from the setup is also not an option, as moving any optical component can

shift the image or move the focal plane of the setup, thus altering the calibrated properties.

In order to calibrate the setup, an array of 30×30 holes of $30 \mu\text{m}$ diameter was placed at the Schupmann focus of the telescope. The resulting pattern of point sources on the camera CCDs is wavelength dependent only through the diffraction pattern, which can be accurately modeled and which does not affect the position of the pinholes.

We need to find out the differences between different channels, i and k . First we find the tilts between all the object focus channels by processing them with a reduced set of modes, only Zernike tilt modes, and no constraints except for the JPDS tilt constraints (Eq. (9b)). The pinhole array was designed to give one pinhole every 200 pixels (without re-imaging), so that we have no more than one pinhole for each subfield. The reduced tilt coefficients are converted to physical shifts for each pixel and stored in an offset file, which is used to align the subfields and calculate a starting value for the tilt coefficients. This process is repeated until the corrections to the tilt coefficients are sufficiently small. In this way it is also possible to remove other types of misalignments that can, to first order, be approximated by local translations, such as rotations and image scale differences, provided they are small.

It remains important to minimize the relative rotation of the cameras in the image plane, as the rotation itself cannot be modeled by wavefront distortions and, if severe, may result in inaccurate restorations.

Next are the diversities and tilts for the PD setups. This is done by restoring the pinhole images with a reduced set of modes, $\mathcal{M}_{\text{reduced}}$, usually consisting of Zernike tilt and focus modes, and no constraints except for the JPDS tilt constraints (Eq. (9b)). All PD setups are calibrated independently, but including the tilts determined in the first step for the focus channel. We now have approximate values for tilt and focus for all channels in the setup with respect to the focus channels. In principle, more fixed aberrations can be added to $\mathcal{M}_{\text{reduced}}$ and absorbed in the θ_{ij} (e.g. spherical aberration, coma, etc.), if they are known to be originating from the setup.

In our data, most of the remaining aberrations could be attributed to small imperfections in the shape of the AO mirror, which, although fixed in the pinhole images, are not fixed for variable seeing conditions. Therefore, they were not included in the θ_{ij} .

The previous step is applied iteratively, until the corrections to the fixed aberrations have become sufficiently small.

In the final step, with the calculated approximate focus diversities and tilts loaded into the appropriate θ_{ij} , the full KL parameterization is solved on a good quality solar image data set, for each object

independently. This is necessary, as the pinhole images are not very suitable for wavefront sensing of higher order modes, often leading to confusion of one mode for a combination of other ones. Allowing for variable seeing, we require that the fixed aberration and registration differences between object channels be constant over time,

$$\alpha_{i11m} - \alpha_{it1m} = \alpha_{i1km} - \alpha_{itkm}; \quad t > 1, k > 1, m \in \mathcal{M}_{\text{reduced}}, \quad (13a)$$

for the reduced set of modes we want to model. For all other modes we require that they are the same for all wavefront realizations,

$$\alpha_{it1m} = \alpha_{itkm}; \quad k > 1, m \notin \mathcal{M}_{\text{reduced}}. \quad (13b)$$

Again, the tilts are constrained to sum to zero,

$$\sum_t \alpha_{it1m} = 0; \quad m \in \mathcal{M}_{\text{tilts}}. \quad (13c)$$

The remaining aberrations found in this step are added to the θ_{ij} and used in the processing described in the following sections. Corrections of the tilt coefficients should only be made to the diversity channels, as otherwise the alignment achieved in the first step is destroyed.

4.3. BLUE BEAM

Two spectral bands of interest are the G-band at 430.5 nm and the nearby continuum at 436.4 nm. Since they are at the blue end of the solar spectrum, they provide a high spatial resolution and contrast. Furthermore, magnetic structures show up as bright points in the G-band, making this a convenient diagnostic to study the dynamics of magnetic elements (see e.g. Carlsson et al. (2004) and Shelyag et al. (2004), for recent discussions on the G-band as a magnetic proxy).

The proximity of these two bands to each other makes it possible to assume that the atmospheric wavefront distortions are to a good approximation the same for both. As the images taken in the G-band and the G-cont look quite different, the effects of the atmospheric wavefront distortions is different. This makes it easier to separate the atmospheric distortions from real image features, when they are reduced together.

The G-band and the G-cont were observed together with the Ca II H line. Since the wavelength of the Ca II H line is just beyond the reach of the normal KAF1600 CCDs, a blue-sensitive CCD is needed, which was only available in the form of a 6.3 megapixel camera.

The setup used in this section is shown in figure 2 (right). Several different types of cameras were used in the setup. The 1.6 and 4.2 megapixel cameras were run at the same frame rate, approximately 1.8

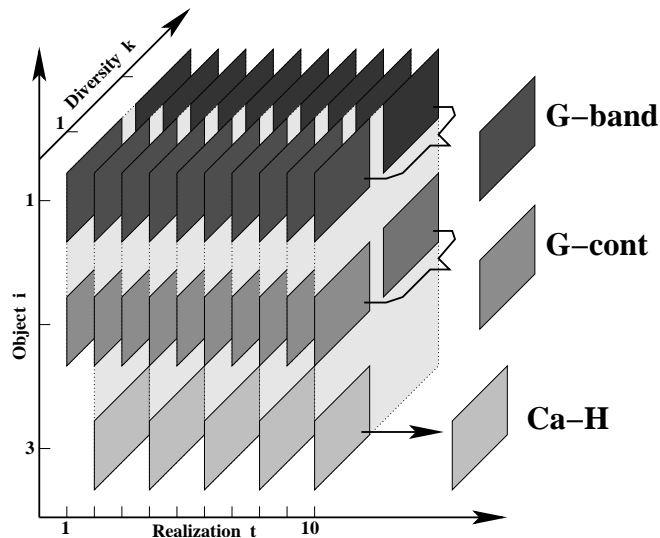


Figure 3. Linear equality constraints for the blue beam setup. Wavefront coefficients are constrained to be the same for all objects. Ca II H does not have a diversity channel and is only available for even realization index t .

frames/s, and the even slower 6.3 megapixel Ca II H camera at half of that, approximately 0.9 frames/s. Only one Ca II H frame was therefore available for every 2 frames of the other cameras.

The shutter time was ~ 10 ms for all cameras.

Linear Equality Constraints

We have $\mathcal{T}_{\text{G-band}} = \mathcal{T}_{\text{G-cont}} = \{1, 2, \dots, 10\}$ and $\mathcal{T}_{\text{Ca II H}} = \{2, 4, \dots, 10\}$. This can be conveniently included in the linear equality constraints, as illustrated in Figure 3. Both the G-band and G-cont objects have a diversity channel and the same number of wavefront realizations. The Ca II H channel has no diversity camera and is running at half the frame rate and thus the frames are linked only to the even frames of the other cameras.

Small registration errors, resulting from small camera alignment errors, are quantified with the calibration procedure from section 4.2 and absorbed in θ_{ij} . We can then require that the coefficients of the pupil phases are equal for the different objects,

$$\alpha_{1t1m} - \alpha_{itkm} = 0; \quad (i, k) \neq (1, 1), m \in \mathcal{M}, \quad (14a)$$

as well as the additional registration constraints Eq. (9b).

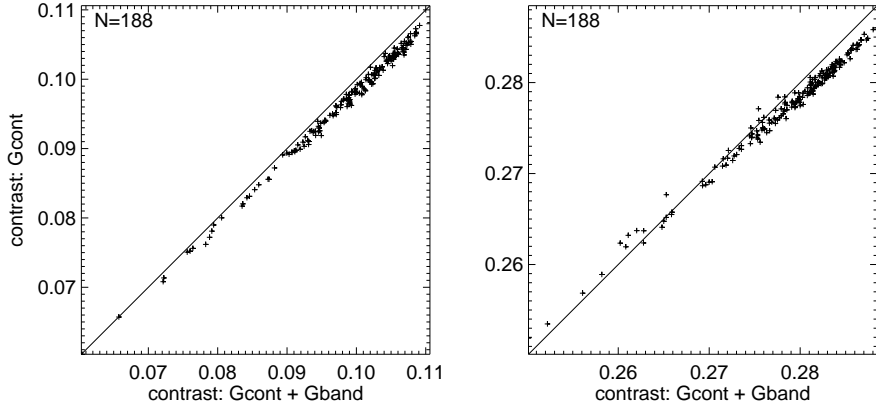


Figure 4. Contrast numbers for G-cont + G-band vs G-cont only for an area with only granulation (**left**) and an area with a sunspot (**right**), for 188 independent sets of $T = 8$ realizations each.

G-band PD + G-cont PD

We used 128×128 pixel subfields with a modified Hanning window with an 8 pixel cosine incline from zero to unity, corresponding to an undisturbed field of view (FOV) of $5'' \times 5''$. This should make the isoplanatic approximation valid. The frames were divided into subfields on a 64-pixel grid, allowing ample overlap for seamless mosaicking. The number of modes used was gradually increased from a starting value of 5 to a final value of 34, incremented in steps of 5.

Contrary to Löfdahl (2002), who used only 3 PD pairs, for the 10 PD pairs multi-object restorations we found that the quality of the final restored object improved if we based it on all the data, and not on the focused data only. This may be due to the lower signal level resulting from the large number of cameras over which the light was divided and the large number of frames, due to which the PSFs are more accurately determined.

In an attempt to quantify the effect of multi-object restoration, we have compared the contrasts in G-cont object estimates from ordinary PDS (i.e. a single object) with the corresponding numbers from a multi-object restoration involving both G-cont and G-band PD data.

In figure 4 we show two scatter plots where 1-object contrasts are plotted against 2-object contrasts, for a set of images with variable seeing quality. Two cases are considered: granulation with magnetic bright points and a sunspot. The contrast is defined as

$$C = \frac{\sqrt{\langle \hat{f}_i^2 \rangle - \langle \hat{f}_i \rangle^2}}{\langle \hat{f}_i \rangle}, \quad (15)$$

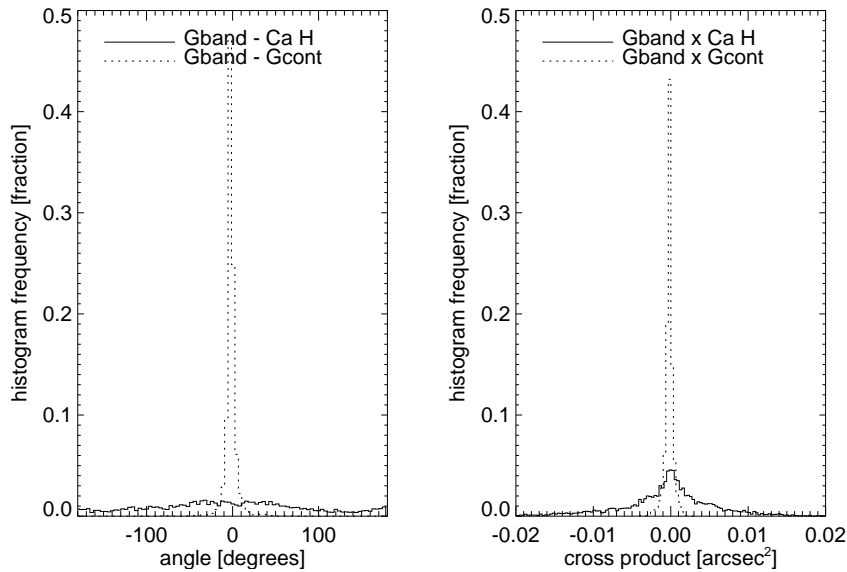


Figure 5. Difference in differential seeing between G-cont and Ca II H. The left panel shows a histogram of the relative angles between offset vectors. The right panel shows a histogram of the vector lengths of the cross-products of the offset vectors.

where the angular brackets denote spatial averages over a 442×948 -pixel ($18'' \times 38''$) subfield for the granulation with magnetic bright points and 736×796 -pixel ($30'' \times 32''$) subfield for the sunspot. An expected linear correlation can clearly be seen in both plots, simply indicating that good seeing produces higher contrast. It is just as clear that 2-object restoration boosts the contrast in a majority of the images, with some exceptions in the bad-seeing end of the sunspot data set.

An increase in contrast could theoretically result from over-compensation by suboptimal wavefront phases. However, a contrast increase because of badly estimated wavefronts would be expected to dominate for low contrast data, contrary to what is observed in the figure. For the granulation FOV, the contrast increase is about the same regardless of the seeing and for the sunspot FOV there is a linear relation that favors good seeing data. We conclude that the multiple-objects approach results in better determined wavefront phases, that help restoring real contrast in the images.

G-band PD + G-cont PD + Ca II H

Since G-band and G-cont are only 6 nm apart in wavelength, it is likely that the images taken in these bands can be simultaneously reduced. For the Ca II H line, this is not quite as obvious, as the wavelength

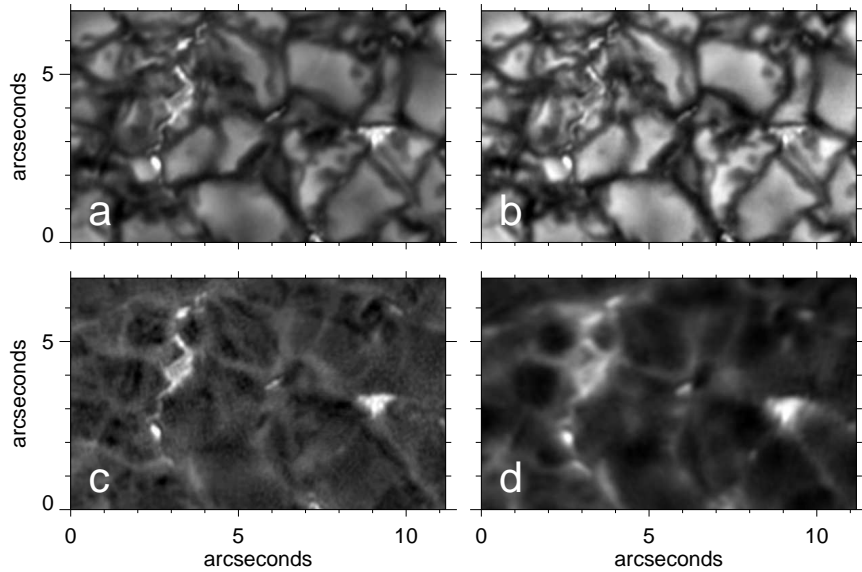


Figure 6. a: G-band, b: G-cont, c: G-band-G-cont difference image, d: 0.11 nm FWHM image centered on 396.78 nm in the wing of Ca II H, 70 pm from line center.

difference between the G-cont and the Ca II H line is approximately 35 nm. Wavelength dependences of the refractive index could perhaps have been addressed with an approach similar to that of Tritschler and Schmidt (2002a), who used separate scaling laws for atmospheric and telescopic aberrations. However, the main problem with including the Ca II H data in the joint processing appears to be geometrical distortions from anisoplanatism.

If a comparison between the alignment of raw data images is made, it quickly becomes obvious that the differential seeing of Ca II H and G-cont images is not identical. In an experiment to illustrate this effect, we determined the relative change in position of sub-areas of consecutive raw images in the G-band, G-cont and Ca II H. The offset vectors, obtained from cross-correlating $4'' \times 4''$ square sub-images, are a measure of the differential seeing in the different spectral regions. In figure 5, a comparison is made between the offset vectors of the G-band and Ca II H, and between G-band and G-cont: the left panel shows the histogram of the relative angles between offset vectors of corresponding sub-images in the different filters, the right panel shows the cross-product of the offset vectors. The histograms clearly show that the differential seeing for G-band and G-cont is very similar: relative angles are very small and the values of the cross-products are small. For G-band vs. Ca II H, the relative angles are distributed

evenly across the whole range, and the values of the cross-products are significantly spread around zero, illustrating that the differential seeing for the Ca II H filter is very different from that in the G-band spectral region. Good alignment between restored objects can therefore not be achieved.

It is not clear, however, that this means that no improvement can be obtained at all by joint restoration. Further testing using Ca II H PD data, obtained with a different setup, and simultaneous G-band data showed that the wavefront sensing is indeed more stable and results in fewer image artifacts in the Ca II H images using both Ca II H and G-band than when using only Ca II H images, when the seeing is excellent. When the seeing is not very good, however, joint restoration of the 2 objects results in significantly worse restorations for both the Ca II H and G-band than for the 2 objects restored separately.

Since less than excellent seeing results in decreased quality of the restorations for all the objects in the set, it appears that multi-object restorations are not the preferred method of image restoration for this particular combination of filters. Clearly, to improve the Ca II H restoration by adding multi-object information, a filter that is closer in wavelength to Ca II H will need to be used.

Figure 6 shows a detail of a quiet area in G-band, G-cont, and Ca II H, simultaneously restored using a 3-object MOMFBD set (see figure 3). Since the seeing was very good, all restored images are of excellent quality. Moreover, since the seeing for the G-band and G-cont images is identical, they are aligned by construction. This can be used to subtract the G-cont from the G-band image to create a “magnetic difference” (Berger et al., 1998) image as shown in panel c. The alignment is to sub-pixel accuracy, further alignment and de-stretching to match G-cont to G-band is not required.

4.4. SOUP RESULTS

As illustrated in the left panel of figure 2, the setup for the red beam makes use of the SOUP filter (Title and Rosenberg, 1981). The SOUP filter is a tunable birefringent Lyot filter with a bandpass of about 8 pm for the Fe I 630.2 nm spectral line, and about 12.8 pm for H- α (in ‘wide’ mode). The SOUP filter is equipped with 2 Liquid Crystal Variable Retarders (LCVRs) which are used to make longitudinal Stokes-V magnetograms in the Fe I 630.2 line. The free spectral range of SOUP is about 0.8 nm, a set of broad-band interference filters (of FWHM 0.8 nm) is used as blocking filters. We used 15 ms exposures and a frame rate of approximately 3.5 frames/s.

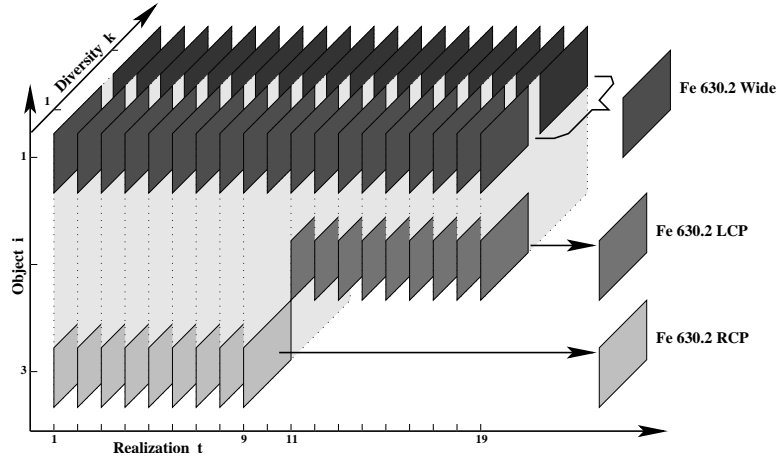


Figure 7. Linear equality constraints for the red beam setup. Simultaneous wavefront coefficients are constrained to be identical. Objects 2 and 3 (Fe 630.2 nm RCP and LCP) both don't have a diversity channel, they are aligned to object 1 (Fe 630.2 nm wide) and therefore to each other.

Linear Equality Constraints

The low transmission ($\approx 10\%$) and the small bandwidth of the SOUP filter in combination with the fact that we operate close to the line core of strong spectral lines, results in very low light levels. If exposure times are to stay below the seeing-freezing time, an additional reduction of the signal level for phase diversity wavefront sensing would result in unacceptably noisy data. In addition, the filter can only assume one position at a time, so that recording images in more than one filter position simultaneously is not possible. As we want to do PD restoration on the filtered images and we want images from different filter positions to be accurately aligned, another 2 cameras were added by splitting off 10% of the light before the tunable filter but after the optical chopper so that these images are recorded strictly simultaneously with the SOUP filter images. These cameras share the same 0.8 nm wide filter that is used as blocking filter for the SOUP filter so that the seeing properties are identical for all 3 cameras. The fact that these PD cameras look at a single object while the SOUP camera object is switched by the tuning of the SOUP and/or the changing of the polarizers, makes it possible to link also the latter to each other (as illustrated in figure 7). In addition, a "free" extra imaging channel results from the PD restorations, which, in the case of the Fe 630.2 nm filter corresponds to an image that is dominated by the continuum.

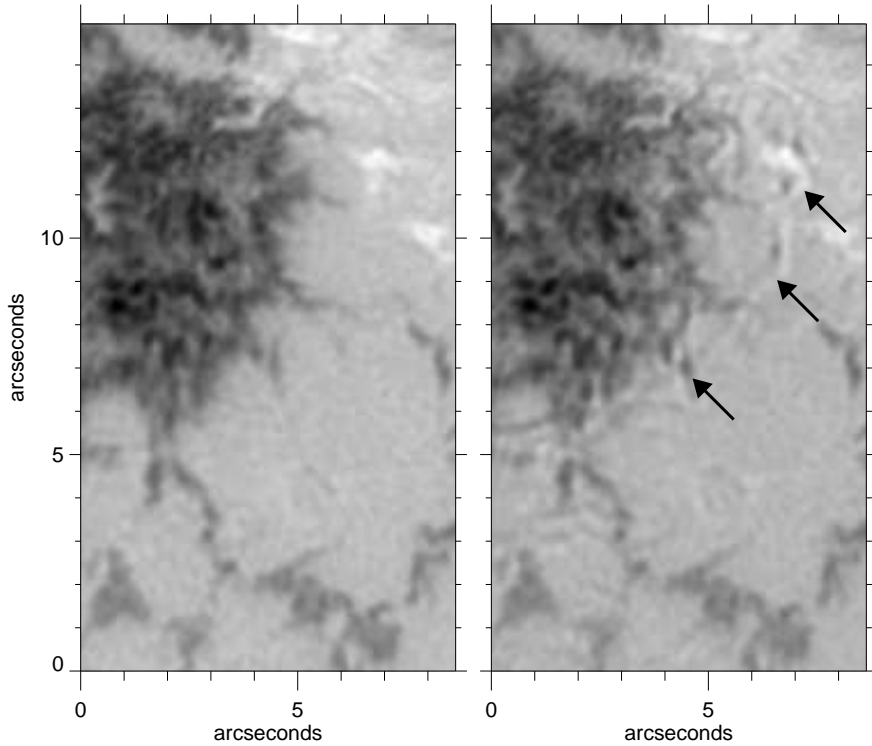


Figure 8. Fe I 630.2 nm magnetograms made from -6 pm RCP and LCP images. The left panel shows a magnetogram made from simultaneously restored RCP and LCP images. The right magnetogram is made from separately restored RCP and LCP images which were aligned by sub-image cross-correlation and destretching. Arrows mark clear examples of spurious signals from alignment mismatches.

We have $\mathcal{T}_{\text{wideband}} = \{1, 2, \dots, 19\}$, $\mathcal{T}_{\text{LCP}} = \mathcal{T}_{\text{RedWing}} = \{1, 2, \dots, 9\}$ and $\mathcal{T}_{\text{RCP}} = \mathcal{T}_{\text{BlueWing}} = \{11, 12, \dots, 19\}$. Constraints are of the same type as for the blue beam, Eq. (14a) and (9b).

Not only can sub-pixel alignment be achieved for images degraded with completely independent wavefront realizations, also wavefront information retrieved from the extra two cameras can be used to restore tunable-filter objects, which might otherwise not be suitable for wavefront sensing due to a low signal to noise ratio and/or a low image contrast.

Even though residual large scale deformations of the images are not completely absent, they are guaranteed to be the same for all restored objects in the set.

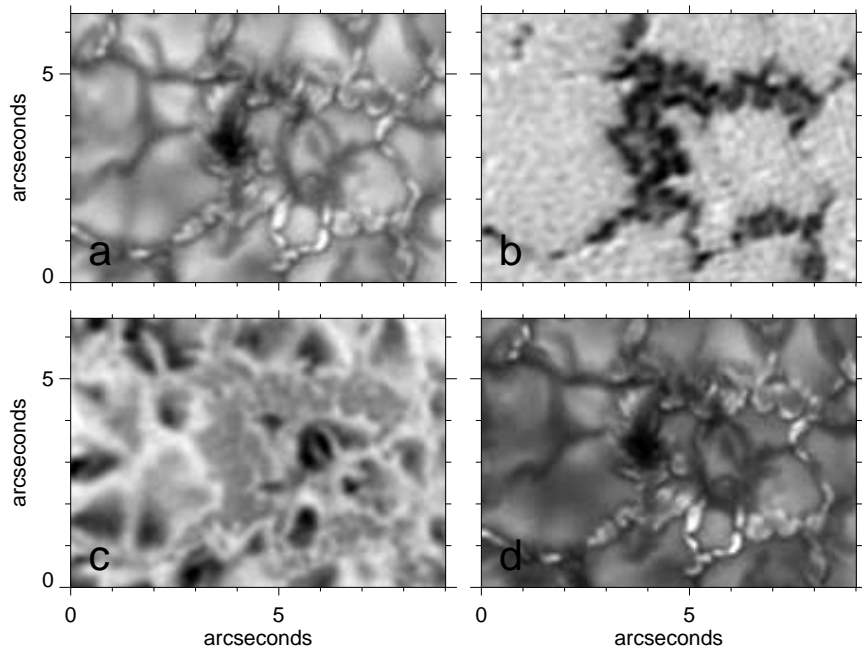


Figure 9. a: 0.8 nm wide image centered on 630.2 nm. b: Fe I 630.2 magnetogram. c: Fe I 630.2 Dopplergram. d: G-band image.

Magnetograms and Dopplergrams

Some observables of interest are magnetic field strength and line of sight velocities. When calculating these quantities from observations made using the SOUP filter, non-simultaneously taken images need to be subtracted, for which large scale atmospheric distortions are a major problem.

Alignment of the images is made difficult by the fact that the images to be subtracted usually look very different and are therefore hard to correlate. This can result in artificial signals or loss of real signals, caused by regions with steep intensity gradients not being accurately aligned before subtraction. With the setup described above, this problem can be virtually eliminated, by reducing all the data as a single MOMFBD set.

As in section 4.3, we used 128×128 pixel subfields with a modified Hanning window with an 8 pixel cosine incline from zero to unity. Due to the different image scale, this now corresponds to an undisturbed FOV of $7'' \times 7''$. The number of modes used was the same as in section 4.3, with a starting value of 5 and a final value of 34 modes, increased in steps of 5.

Figure 8 shows details from two magnetograms of an active region observed during good-seeing conditions. The left magnetogram is constructed from RCP and LCP images which were restored simultaneously using the procedure described above. The right magnetogram is constructed from the same raw RCP and LCP exposures but using a more traditional approach: the RCP and LCP images were restored separately, aligned to each other using sub-image cross-correlation and destretching and then subtracted. Clearly, the noise resulting from the subtraction of inaccurately aligned convection cells, visible in the traditionally reduced data, is almost absent in the MOMFBD reduced data.

Since the reduced reference images are also accurately aligned with the magnetograms, a detailed comparison can be made between the magnetic structures and their continuum counterparts. Systematic offsets, previously indistinguishable from artificial offsets, can now be interpreted as definitively real. Figure 9 shows a continuum image, a magnetogram and a Dopplergram obtained from simultaneously reduced exposures. A co-temporal G-band image which was not restored from the same MOMFBD set is also shown. Clear examples are visible of small-scale magnetic structures in the form of bright points and more extended structures like a micro-pore and ribbons, see also Berger et al. (2004) and Rouppe van der Voort et al. (2005).

We are using polarized data from a magnetically sensitive line to construct the Dopplergrams, so it is necessary to use images for both polarizations on both sides of line center to get reliable velocity data. This was done by extending the constraints from Figure 7 from 3 to 5 objects, totaling 110 images. The total time spanned by this kind of image set is pushing the time limits imposed by the solar evolution time.

The grainy pattern in the magnetogram is the result of the low signal level, caused by the short exposure times in combination with a modest frame rate. Closer examination of the sensitivity of the magnetogram shows that the noise level corresponds well to that of a magnetogram with an exposure time equal to the sum of the exposure times of the images used in the MOMFBD restorations. This problem can therefore be reduced by using more images taken at a higher frame rate.

H- α Core and Dopplergrams

In the core of H- α , the signal level is so low that the images are dominated by photon noise. This presents a new challenge, as the only way to increase the signal is to expose longer, which is not possible while staying below the seeing-freezing time. Furthermore, the assumption of Gaussian noise is increasingly less accurate with decreasing signal

level, so that for an accurate treatment, great care needs to be taken in estimating the noise level.

Figure 10 shows a detail of AR662 of an image recorded with a 0.8 nm wide filter centered on the wavelength of H- α (656.3 nm), a 12.8 pm wide line core image and a Dopplergram, constructed from exposures at +30 pm and -30 pm from line center. Comparisons between joint and separate restorations show clearly that the joint restoration of the broadband image and the narrowband image benefit the narrowband image, and the influence of noise appears to be quite small.

Compared to the Fe 630.2 images, the restorations appear to be more sensitive to the quality of the raw data. Moderately degraded images do not improve as much as expected from the Fe 630.2 data, and severely degraded images even show a "blocked" pattern in the image, caused by a difference in the average signal level of the subfields.

This problem is partially caused by an underestimated noise level, possibly due to the incorrect assumption of Gaussian statistics for photon noise, and can be decreased by multiplying the estimated noise level by an experimentally determined factor.

Although simulations with noisy data confirm that the main result of adding noise to degraded images is loss of detail in the restored images, it is not clear whether the problem described above is due only to the high noise level or the incorrect assumptions about the statistics of the photon noise. It is also possible that the contrast in the images recorded with the 0.8 nm H- α filter is not as suitable for wavefront sensing as that of images taken in the continuum.

The property of accurate alignment by construction between the broadband and the narrowband images is clearly an advantage for this type of data, as aligning them on the basis of recognizable features is virtually impossible. Also the reliable alignment of the red and blue wing images in the Dopplergram is greatly facilitated by the simultaneous reduction and would be very difficult to achieve by any other means.

5. Conclusion

We have presented a new generalization of MFBD by extending it to include multiple objects. We have demonstrated that simultaneous reduction of multiple object data can improve the restorations of all objects over single-object restorations, provided the filters used in the optical setup are sufficiently close in wavelength.

With accurate calibration and simultaneous wavefront sensing, the identical deconvolution of the raw data with the multi-object method

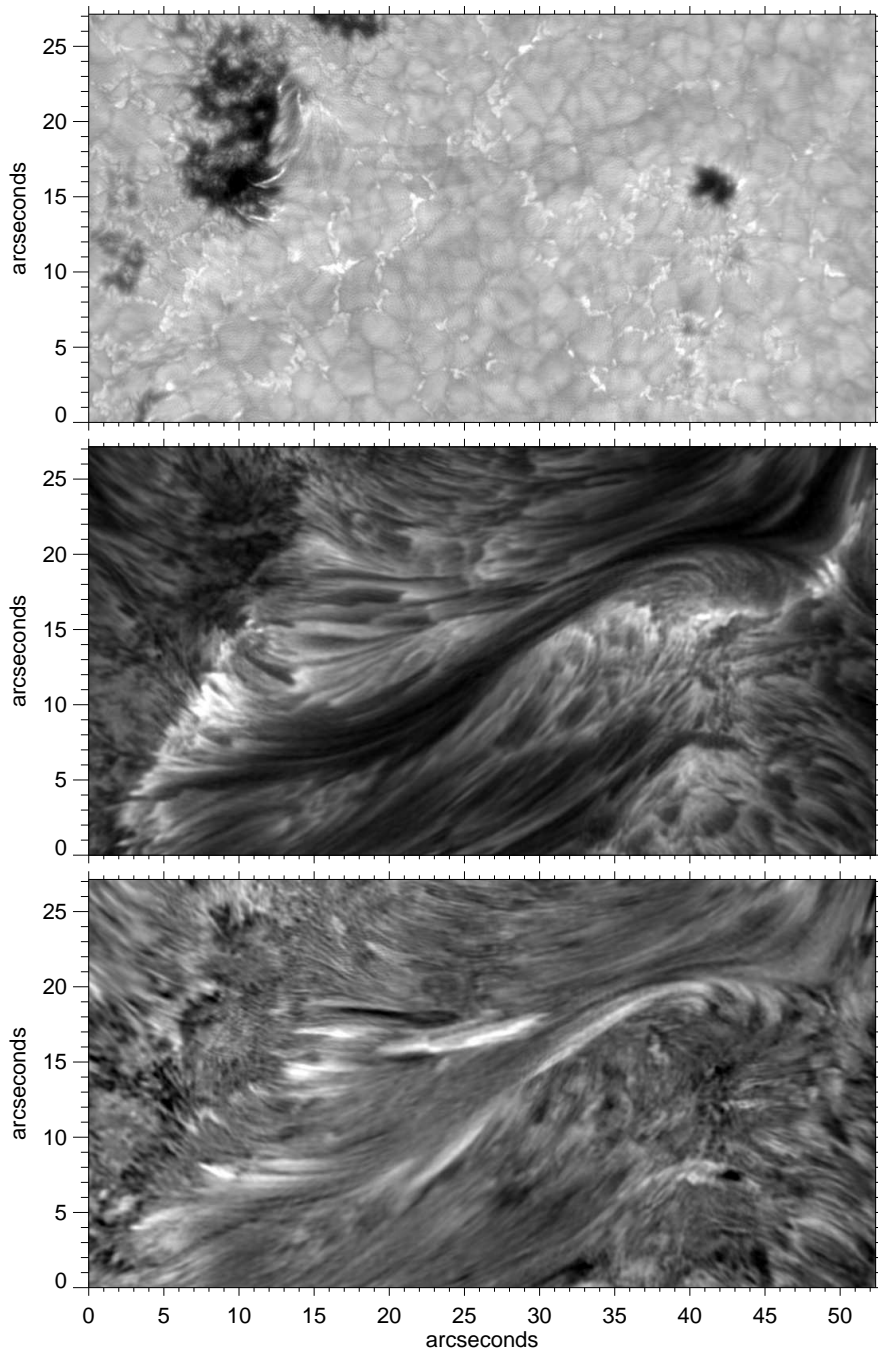


Figure 10. Detail of AR662 on August 21, 2004, containing a small filament. The top panel shows a wide band image centered on H- α , the middle panel H- α line center, the bottom panel an H- α Dopplergram with positive values corresponding to downward velocity and white in the image.

results in near perfect alignment of objects. This can be achieved both for simultaneously and for non-simultaneously observed objects, as long as they can be linked through at least one extra, simultaneously observed object.

The MOMFBD formulation in combination with an external shutter make a versatile tool for solar observations as demonstrated by the ability to model and process data from our varied setups with different cameras, filters, polarizers, etc. The method has proven to be robust, even for very noisy data, although improvements are needed to treat non-Gaussian noise correctly.

Acknowledgements

This research was supported by the European Community's Human Potential Programme through the European Solar Magnetism Network (ESMN, contract HPRN-CT-2002-00313), from The Research Council of Norway through grant 146467/420, through a grant of computing time from the Programme for Supercomputing, through a grant of computing time by participation in the CONDOR GRID computing project of the University of Oslo, and by NSF under grant IIS ITR 03-24816. The Swedish 1-m Solar Telescope is operated on the island of La Palma by the Institute for Solar Physics of the Royal Swedish Academy of Sciences in the Spanish Observatorio del Roque de los Muchachos of the Instituto de Astrofísica de Canarias. We thank the staff of the SST including Göran Scharmer, Peter Dettori, Rolf Kever, Roy Henderson, and Göran Hosinsky for assistance in all aspects of the observations. The Solar Physics group of Lockheed Martin and in particular Tom Berger is thanked for reviving and modernizing the SOUP filter.

References

- Al, N., C. Bendlin, J. Hirzberger, F. Kneer, and J. Trujillo Bueno: 2004, 'Dynamics of an enhanced network region observed in $H\alpha$ '. *Astronomy & Astrophysics* **418**, 1131–1139.
- Berger, T., L. Rouppe van der Voort, M. Löfdahl, M. Carlsson, A. Fossum, V. Hansteen, E. Marthinussen, A. Title, and G. Scharmer: 2004, 'Solar Magnetic Elements at 0.1 arcsec Resolution. General appearance and magnetic structure'. *A&A* **428**, 613–628.
- Berger, T. E., M. G. Löfdahl, R. A. Shine, and A. M. Title: 1998a, 'Measurements of Solar Magnetic Element Dispersal'. *Astrophysical Journal* **506**, 439.
- Berger, T. E., M. G. Löfdahl, R. A. Shine, and A. M. Title: 1998b, 'Measurements of Solar Magnetic Element Motion from High Resolution Filtergrams'. *Astrophysical Journal* **495**, 973.

- Berger, T. E., M. G. Löfdahl, R. S. Shine, and A. M. Title: 1998, ‘Measurements of Solar Magnetic Element Motion from High-Resolution Filtergrams’. *ApJ* **495**, 973.
- Carlsson, M., R. F. Stein, Å. Nordlund, and G. B. Scharmer: 2004, ‘Observational Manifestations of Solar Magnetoconvection: Center-to-Limb Variation’. *ApJL* **610**, L137–L140.
- de Boer, C. R., F. Kneer, and A. Nesis: 1992, ‘Speckle observations of solar granulation’. *Astronomy & Astrophysics* **257**, L4.
- Denker, C., D. Mascarinas, Y. Xu, W. Cao, G. Yang, H. Wang, P. R. Goode, and T. Rimmele: 2004, ‘High-Spatial Resolution Imaging Combining High-Order Adaptive Optics, Frame Selection, and Speckle Masking Reconstruction’. *Solar Physics*. In press.
- Denker, C., G. Yang, and H. Wang: 2001, ‘Near Real-Time Image Reconstruction’. *Solar Physics* **202**, 63.
- Dionne, C. E. and R. A. Gonsalves: 2004, ‘Imaging through an optical waveguide with wavelength diversity’. *Optics Express* **43**(2), 445–449.
- Frigo, M. and S. G. Johnson: 2005, ‘The Design and Implementation of FFTW3’. *Proceedings of the IEEE* **93**(2), 216–231. special issue on.
- Gonsalves, R. A.: 1982, ‘Phase retrieval and diversity in adaptive optics’. *Optical Engineering* **21**(5), 829–832.
- Ingleby, H. R. and D. R. McGaughey: 2005, ‘Real data results with wavelength-diverse blind deconvolution’. *Optics Letters* **30**(5). In press.
- Janßen, K., A. Vögler, and F. Kneer: 2003, ‘On the fractal dimension of small-scale magnetic structures in the Sun’. *Astronomy & Astrophysics* **409**, 1127–1134.
- Kahaner, D., C. Moler, and S. Nash: 1989, *Numerical Methods and Software*. Prentice Hall.
- Keller, C. U.: 1992, ‘Resolution of Magnetic Flux Tubes on the Sun’. *Nature* **359**, 307–308.
- Keller, C. U. and O. von der Lühe: 1992, ‘Solar Speckle Polarimetry’. *Astronomy & Astrophysics* **261**, 321–328.
- Kelley, C. T.: 1999, *Iterative methods for optimization*, Frontiers in applied mathematics. Philadelphia, PA, USA: SIAM.
- Löfdahl, M. G.: 2002, ‘Multi-frame blind deconvolution with linear equality constraints’. In: P. J. Bones, M. A. Fiddy, and R. P. Millane (eds.): *Image Reconstruction from Incomplete Data II*, Vol. 4792 of *Proc. SPIE*. pp. 146–155.
- Löfdahl, M. G., T. E. Berger, R. A. Shine, and A. M. Title: 1998, ‘Preparation of a Dual Wavelength Sequence of High-Resolution Solar Photospheric Images using Phase Diversity’. *Astrophysical Journal* **495**, 965–972.
- Löfdahl, M. G. and G. B. Scharmer: 1994, ‘Wavefront Sensing and Image Restoration from Focused and Defocused Solar Images’. *Astronomy & Astrophysics Supplement Series* **107**, 243–264.
- Noll, R. J.: 1976, ‘Zernike Polynomials and Atmospheric Turbulence’. *Journal of the Optical Society of America* **66**(3), 207–211.
- Paxman, R. G., T. J. Schulz, and J. R. Fienup: 1992a, ‘Joint estimation of object and aberrations by using phase diversity’. *Journal of the Optical Society of America A* **9**(7), 1072–1085.
- Paxman, R. G., T. J. Schulz, and J. R. Fienup: 1992b, ‘Phase-Diverse Speckle Interferometry’. In: *Signal Recovery and Synthesis IV*, Vol. 11 of *Technical Digest Series*. pp. 5–7.

- Paxman, R. G., J. H. Seldin, M. G. Löfdahl, G. B. Scharmer, and C. U. Keller: 1996, 'Evaluation of Phase-Diversity Techniques for Solar-Image Restoration'. *Astrophysical Journal* **466**, 1087–1099.
- Rimmele, T. R.: 2000, 'Solar adaptive optics'. In: P. L. Wizinowich (ed.): *Adaptive Optical Systems Technologies*, Vol. 4007 of *Proc. SPIE*. pp. 218–231.
- Roddier, N.: 1990, 'Atmospheric wavefront simulation using Zernike polynomials'. *Optical Engineering* **29**(10), 1174–1180.
- Rouppe van der Voort, L. H. M., V. H. Hansteen, M. Carlsson, A. Fossum, E. Marthinussen, M. van Noort, and T. E. Berger: 2005, 'Solar magnetic elements at 0.1 arcsec resolution. II dynamical evolution'. *A&A*. *submitted*.
- Rouppe van der Voort, L. H. M., M. G. Löfdahl, D. Kiselman, and G. B. Scharmer: 2004, 'Penumbra structure at 0''.1 resolution. I. General appearance and power spectra'. *Astronomy & Astrophysics* **414**, 717–726.
- Rutten, R. J., R. H. Hammerschlag, F. C. M. Bettonvil, P. Sütterlin, and A. G. de Wijn: 2004, 'DOT tomography of the solar atmosphere. I. Telescope summary and program definition'. *Astronomy & Astrophysics* **413**, 1183–1189.
- Sütterlin, P., L. R. Bellot Rubio, and R. Schlichenmaier: 2004, 'Asymmetrical appearance of dark-cored filaments in sunspot penumbrae'. *Astronomy & Astrophysics* **424**, 1049–1053.
- Sailer, M., O. von der Lühe, and F. Kneer: 2004, 'Adaptive Optics Transfer Function Estimation for Solar Observation'. *Astronomische Nachrichten* **325**(S1), 130.
- Scharmer, G. B., K. Bjelksjö, T. K. Korhonen, B. Lindberg, and B. Petterson: 2003a, 'The 1-meter Swedish solar telescope'. In: S. L. Keil and S. V. Avakyan (eds.): *Innovative Telescopes and Instrumentation for Solar Astrophysics*, Vol. 4853 of *Proc. SPIE*. pp. 341–350.
- Scharmer, G. B., P. M. Dettori, M. G. Löfdahl, and M. Shand: 2003b, 'Adaptive optics system for the new Swedish solar telescope'. In: S. L. Keil and S. V. Avakyan (eds.): *Innovative Telescopes and Instrumentation for Solar Astrophysics*, Vol. 4853 of *Proc. SPIE*. pp. 370–380.
- Scharmer, G. B., B. V. Gudiksen, D. Kiselman, M. G. Löfdahl, and L. H. M. Rouppe van der Voort: 2002, 'Dark cores in sunspot penumbral filaments'. *Nature* **420**, 151–153.
- Scharmer, G. B., M. Shand, M. G. Löfdahl, P. M. Dettori, and W. Wei: 2000, 'A Workstation Based Solar/Stellar Adaptive Optics System'. In: P. L. Wizinowich (ed.): *Adaptive Optical Systems Technologies*, Vol. 4007 of *Proc. SPIE*. pp. 239–250.
- Schulz, T. J.: 1993, 'Multi-Frame Blind Deconvolution of Astronomical Images'. *Journal of the Optical Society of America A* **10**, 1064–1073.
- Shelyag, S., M. Schüssler, S. K. Solanki, S. V. Berdyugina, and A. Vögler: 2004, 'G-band spectral synthesis and diagnostics of simulated solar magneto-convection'. *A&A* **427**, 335–343.
- Shine, R. A., L. Z. Porter, Z. Frank, J. B. Gurman, D. Pothier, and S. Ferguson: 1988, 'A User's Guide to ANA'. Lockheed Palo Alto Research Laboratory. See also <http://ana.lmsal.com>.
- Thelen, B. J., M. F. Reiley, R. G. Paxman, and D. W. Amlin: 1995, 'Fine-Resolution Multispectral Imaging Using Measurement Diversity'. In: *International Symposium on Spectral Sensing Research (ISSSR)*. Melbourne, Australia. <http://ltpwww.gsfc.nasa.gov/ISSSR-95/finereso.htm>.
- Title, A. and W. A. Rosenberg: 1981, 'Tunable Birefringent Filters'. *Optical Engineering* **20**, 815.

- Tritschler, A. and W. Schmidt: 2002a, ‘Sunspot photometry with phase diversity. I. Methods and global sunspot parameters’. *Astronomy & Astrophysics* **382**, 1093–1105.
- Tritschler, A. and W. Schmidt: 2002b, ‘Sunspot photometry with phase diversity. II. Fine-structure characteristics’. *Astronomy & Astrophysics* **388**, 1048–1061.
- Van Kampen, W. C. and R. G. Paxman: 1998, ‘Multi-Frame Blind Deconvolution of Infinite-Extent Objects’. In: L. R. Bissonette (ed.): *Propagation and Imaging through the Atmosphere II*, Vol. 3433 of *Proc. SPIE*. pp. 296–307.
- von der Lühse, O.: 1993, ‘Speckle imaging of solar small structure: I. Methods’. *Astronomy & Astrophysics* **268**, 374–390.
- von der Lühse, O.: 1994, ‘Speckle imaging of solar small structure: II. Study of small scale structure in active regions’. *Astronomy & Astrophysics* **281**(3), 889–910.